

Deep lensing with a twist: E and B modes in a field with multiple lenses

Andrew K. Bradshaw,^{1*} M. James Jee,² J. Anthony Tyson¹

¹*Physics Department, University of California, Davis, 1 Shields Ave., Davis 95616, USA*

²*Department of Astronomy, Yonsei University, 50 Yonsei-ro, Seoul 03722, Korea*

Accepted XXX. Received YYY; in original form ZZZ

ABSTRACT

We explore aperture mass mapping of large scale structures using the E- and B-modes produced in the weak lensing analysis of a field of galaxy clusters in Lynx. Deep multi-color Suprime-cam and *Hubble Space Telescope* imaging data are jointly analyzed to produce estimates of the locations and shear of background galaxies, which are then used to infer the locations and masses of foreground overdensities (E-modes) through the optimal filtering of axisymmetric tangential shears. By approximating this foreground structure of E-modes as a superposition of NFW-like halos, we model the observed ellipticity of each source galaxy as a sum of shears induced by foreground mass structures. We also make maps of the B-modes by similarly filtering the axisymmetric cross shear and show that these B-modes in fact contain information about the cluster masses and locations after identifying several expected sources of B-modes including edge effects, source clustering, and multiple lensing. We verify this reconstruction method using N-body simulation data and demonstrate how the observed B-modes naturally occur when background galaxies are sheared through a cosmic web of lenses.

Key words: cosmology: observations – gravitational lensing: weak – large-scale structure of Universe – galaxies: clusters: general

1 INTRODUCTION

Weak gravitational lensing provides observers with a tool to map and study the large scale mass structure. In the case of a single lensing mass in the foreground, say a cluster of galaxies, weak gravitational deflection of light causes the images of background galaxies to appear tangentially aligned and stretched. Conversely, an under-dense region of space will cause images of distant galaxies to appear radially aligned to the center of the void. Using source galaxies and lenses over a large volume, weak lensing three-dimensional cartography of these mass structures at different redshifts can aid in the understanding of the process of large-scale structure formation.

Observation of the shear signal can be measured on deep CCD images of distant galaxies, as first detected in Tyson et al. (1990). The technique of weak lensing enables the discovery of over-densities (Wittman et al. 2001) and under-densities (Melchior et al. 2014) in surveys. Weak lensing can also be used as a tool to measure masses and profiles of clusters (von der Linden et al. 2014), and it can place statistical constraints on cosmology and the evolution of large scale structure through spatial correlations of the shear (Ba-

con et al. (2000), Kaiser et al. (2000), Van Waerbeke et al. (2000), Wittman et al. (2000), and its tomographic evolution Jee et al. (2016)).

However, this cosmic shear signal is weak and individual galaxies have non-zero intrinsic ellipticities, requiring many background galaxies to be averaged to obtain a high signal-to-noise (S/N) measurement of the shear. For this reason, deep surveys of the sky have been specially designed to maximize the observed number density of background galaxies, decreasing the statistical uncertainty in the measured shear field by the square root of the observed number density of objects. The power of modern weak lensing surveys then depends on the size of the cosmological volume it can probe. Notably, the LSST will have a 5σ depth of $r \sim 27$ (effectively hours of observing time on a 6.7 meter equivalent) across 18,000 square degrees at the end of its nominal 10 year survey. This exposure depth will be achieved by efficiently mosaicking and stacking hundreds of exposures of its 9.6 sq. degree field of view, via an optimal forward model for each object on each CCD. In this paper we use a much smaller region of the sky, but imaged to the full LSST depth, to study the weak lensing shear components induced by the abundance of clustering along the line of sight.

The weak lensing shear is related to the second derivatives of the lensing potential ψ by $\gamma_{ab}(\mathbf{x}) = (\partial_a \partial_b -$

* E-mail: akbradshaw@ucdavis.edu (AKB)

$\frac{1}{2}\delta_{ab}\nabla^2\psi(\mathbf{x})$, which is also known as the tidal field. Using this knowledge, finite field, non-linear reconstruction techniques can then be applied to the measured shears to generate the locations and strengths of lensing potentials on the sky (Bartelmann (1995), Kilbinger (2015)). It was shown in Kaiser (1992) and Stebbins (1996) that in analogy with electromagnetism the vector field representing the shear can be decomposed into two components, namely the electric (so-called E, or gradient, non-vortical, or scalar perturbations) and magnetic (so-called B, curl, vortical, or pseudo-scalar perturbations) shears. Hilbert et al. (2009) argue that to a good approximation lensing produces only E-modes, with B-modes thus an indication of systematic error. Accordingly, foreground density inhomogeneities are the primary source of observable E-mode patterns, while B-modes have been observed to have a much reduced amplitude, variously consistent with zero. Because of the undeniable usefulness of this decomposition to relate E-modes to density perturbations, B-modes have been treated as a contaminant and therefore used as a test of systematic error in the analysis rather than an astrophysical signal. For instance, it was shown in Guzik & Bernstein (2005) that spatially varying calibration errors in excess of 3% r.m.s. would generate B-modes biasing the shape correlation function beyond statistical errors.

However, there are good reasons to investigate B-modes outside of systematics tests. We investigate several interesting sources of B-mode in this paper, using deep observations and simulations in a large volume. It was shown by Schneider et al. (2002) that an inhomogeneous (clustered) distribution of source galaxies can lead to an apparent B-mode. Additionally, if the orientation of background galaxies is non-random (statistical homogeneity and isotropy violation), a B-mode could be present depending on the scale of the intrinsic ellipticity of source galaxies. One example of an anisotropy of source galaxy ellipticity comes from the intrinsic alignment of galaxies expected from direct tidal gravitational interactions of nearby structure, as first detected in Pen et al. (2000). Analytic calculations and simulations of these interactions is complicated however, and predictions of its strength, range, and orientation vary (Joachimi et al. 2013). There also exists a potentially interesting case for generating B-mode if two (or more) lensing clusters are projected along the line of sight, i.e. the double lensing effect as shown in maps of Bertin & Lombardi (2001) and the correlation functions of Cooray & Hu (2002). Finally, there is the possibility of tensor-vector perturbations contributing to both the E- and B-mode (Stebbins 1996), and late time anisotropy has the ability to induce B-modes through coupling of the E-mode and the Weyl tensor (Pitrou et al. 2015). Given the abundance of possible astrophysical sources of B-modes, it is worthwhile to conduct a comprehensive search for B-mode in survey data and in simulations as a potentially useful signal instead of purely an indicator of systematic error.

Of course spurious correlations of observed galaxy shapes can also arise through incorrectly modeled distortions of the point spread function (PSF). For instance, one such PSF distortion comes from the propagation of light through correlated atmospheric refraction patterns, leading to star/galaxy shape correlations depending on the weather and exposure time. Even space-based observations must deal with the tyranny of imperfect optics and detector systematics. For this reason, every weak lensing analysis must address

the issue of PSF modeling. Using stars as a reference for the spurious PSF shear, galaxy images are either deconvolved or forward modeled to produce galaxy shape measurements unbiased by observational conditions.

In this paper we explore the E- and B-modes in 3-dimensional weak lensing via an end-to-end analysis of observational data together with corresponding 3-D simulations of the successive lensing of background galaxies by foreground structures. Identical processing is done for both data and simulations (presented in the appendix), which begins from image data and proceeds through photometric redshift sample selection, shear estimation, aperture mass measurement, and analysis. We reconstruct the observed lensing peaks in the field by estimating their mass and redshift and placing equivalent clusters in the simulation. In this way we can match the observed shear to a sum of successive lensing potentials along the line of sight. Using the maps of the E-mode signal, made by filtering the tangential shear of galaxies around every point, we locate high S/N extended regions and associate them with a mass and redshift using the filtered tangential shear and the redshift clustering of galaxies along the line of light.

In Section 2 we describe our use of the ‘stack-fit’ shape measurement algorithm used on multiple dithered exposures (and multiple bands) to measure the shear in images of varying quality. We also discuss our photometric calibration for color measurements which are used to estimate redshifts in order to separate foreground and background objects. With calibrated shape and redshift information, in Section 3 we describe the detection of clusters in the Lynx field and estimate their masses and redshifts. In Section 4 we use these detected clusters as input to a lensing simulation where we attempt to reproduce the observed shear field, including mass maps and B-modes. We conclude in Section 5 with a summary, and demonstrate our methodology on Λ CDM N -body simulations in the Appendix.

2 DATA AND REDUCTION

The data used in this study consists mainly of Suprimecam 80 megapixel mosaic exposures in Lynx (α : 132.20, δ : +44.93) in the $[B/V/R_c/i'/z']$ filters for [60, 80, 90, 65, 90] minutes on the Subaru telescope during the first observing season in 2001 & 2002. The exposures were dithered during observation, providing a uniform coverage across the field with the large cluster, Lynx North (RX J0848+4456), with a mass $M = 5 \times 10^{14} M_\odot$ and redshift $z = 0.55$ (Holden et al. 2001). Additional super-clustering of galaxies at redshift $z = 1.3$ has been discovered through a combination of X-ray surveys and galaxy clustering (Rosati et al. (1999), Stanford et al. (1997), Mei et al. (2012)). These archival data were gathered from the Subaru-Mitaka-Okayama-Kiso Archive (SMOKA) system (Baba et al. 2002). Raw images were reduced for scientific analysis partially using the SD-FRED1 data reduction process, which provides Suprimecam image overscan and bias subtraction, flat fielding, atmospheric dispersion correction, as well as masking of known bad pixels (Yagi et al. (2002), Ouchi et al. (2004)). Reduced images are then astrometrically aligned using SCAMP (Bertin 2006) by matching to known objects in the Sloan Digital Sky Survey (SDSS) catalogs. The analysis pipeline must fork at

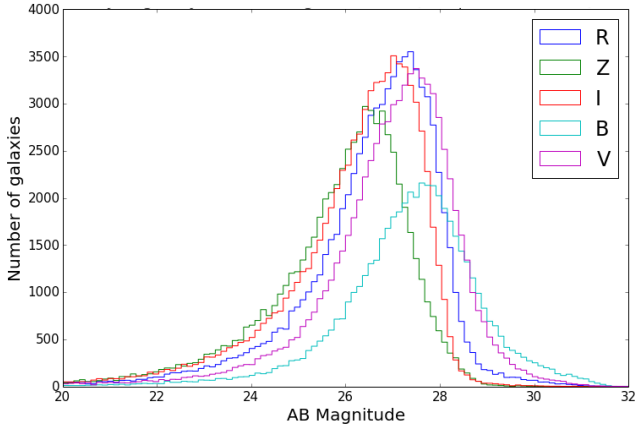


Figure 1. AB magnitude histogram of all Suprime-cam detections (3 or more pixels above 3σ) in the Lynx field, showing completeness to ~ 27 th magnitude, enabling photometric redshift identification of sources at $z > 1.0$.

the step of image combination, because two different criteria must be optimized for weak lensing and photometric analysis.

2.1 Photometric analysis

For photometry, all images in a given $BVR_c i' z'$ filter are PSF matched and coadded using the SDFRED1 pipeline. PSF matched photometry is then performed with ColorPro (Coe & Benítez 2015), where we form a detection image using the deepest and best seeing frames in the R_c, i', z' (reddest) filters, weighted by depth. This detection image is then degraded to individual filters where the seeing is poorer in order to estimate the isophotal flux lost by the degradation. PSF stars for this process are chosen using the same method described below in the shape measurement section 2.2. The degradation of the images is performed using IRAF’s `psfmatch` to determine the kernel by which to convolve the good seeing images to ones of poorer seeing. This process results in a PSF-corrected magnitude that provides robust colors for faint and small galaxies which are close to the noise floor in images (Coe et al. 2006). The resulting photometric catalog is then zero-point calibrated using a combination of matching to SDSS data as well as stellar locus regression (High et al. 2009) to determine precise zeropoint magnitudes across the coadded images. See Figure 1 for the number-magnitude distribution galaxies in the Lynx field.

These well-calibrated zeropoints are essential to ensuring accurate photometric redshift separation of foreground/background objects in lensing scenarios. Our calibrated broadband galaxy colors are photometrically matched to models of redshifted galaxy spectral energy distributions (SEDs) using the Bayesian Photometric Redshifts (BPZ) software (Benítez 2000), which provides estimates of the likelihood of redshift and type, $P(z, t)$, for every object. Some modifications to the defaults were made to improve the magnitude prior as well as updated galaxy SED templates which proved useful in the Deep Lens Survey (Schmidt & Thorman 2013). These tweaks reduced the overall scatter and bias, resulting in $\sigma[(z_p - z_s)/(1 + z_s)] = 0.083$ for all z

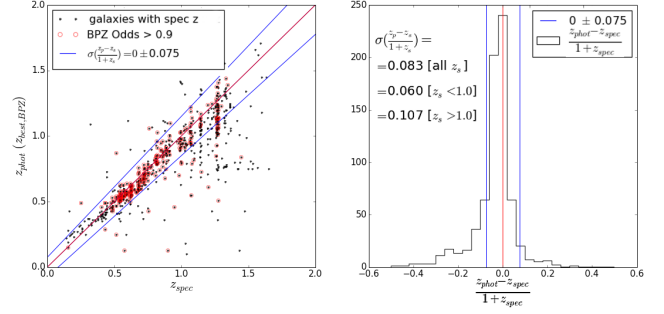


Figure 2. Left: z_{phot} vs. z_{spec} correspondence in the Lynx field, showing good calibration with a few outliers which can be filtered with quality cuts. The vertical band at $z \sim 1.3$ corresponds to the spectroscopically confirmed members of the high redshift super cluster containing Lynx-E, -W, and others. Right: dispersion of the left figure was measured to be $\sigma \sim 0.060$ for $z < 1.0$, implying very complete separation of foreground lenses and background sources.

and $\sigma \sim 0.060$ at $z < 1.0$, as seen in Figure 2. The photometric redshifts are further calibrated for zeropoint offsets using hundreds of high-confidence redshifts from spectroscopic clustering surveying of the field (Mei et al. 2012).

2.2 Shape analysis

For weak lensing analysis, image quality must not be compromised via the above PSF equalization process, which degrades images to match the PSF of the worst seeing filter. We assure that the stacked detection coadds and image analysis for shear measurement take advantage of the best seeing exposures. The V/R/i images are of sufficient PSF quality for weak lensing. In each of these bands, non-PSF matched coadds are produced through SWarp (Bertin et al. 2002), and each image comprising the coadd is then individually analyzed. Preliminary object shape parameters are estimated in addition to the photometric measurements already computed. Stars for PSF estimation are then selected through a combination of filtering and clustering (Figure 3). First, since our field overlaps with SDSS we are able to identify the positions of spectrally confirmed stellar objects, likely including some fraction of binaries unsuitable for PSF analysis. We then use these stars to find the location of the PSF-like objects in our brightness/size diagram (a tilted line due to instrumental “brighter-fatter” or charge transport effects Antilogus et al. (2014)) for each frame, allowing for non-spectrally confirmed PSF-like objects to be gathered. We then further require that these PSF-like objects occupy the 1σ region in color-color (all permutations of $BVR_c i' z'$) space occupied by the spectrally-confirmed objects. We also reject PSF outliers in $e_1 - e_2$ PSF ellipticity space. Objects which pass these criteria are shown as green dots in Figure 3.

The pattern of orientation and ellipticity shown in the whisker plot of Figure 4 is indicative of misalignment and drifting of optical elements during the exposure. Therefore, we model the dozens of PSF stars on each CCD chip and hundreds in each exposure with principal component analysis (PCA) to find the coefficients of twenty “eigenPSFs” for

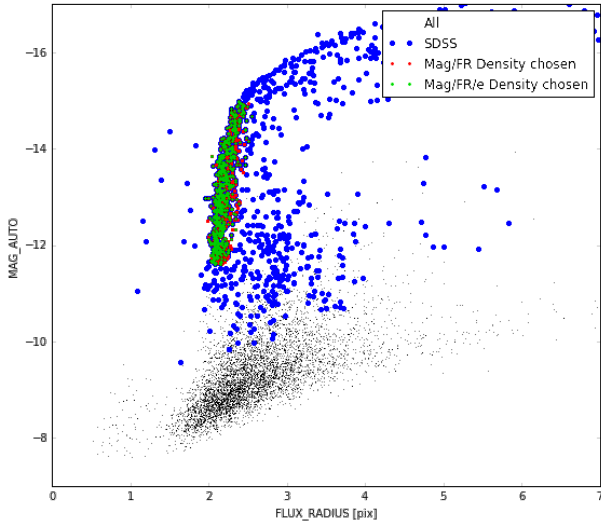


Figure 3. Choosing stars in each exposure to use for PSF modeling. All detected objects, stars and galaxies, are shown as small black points. Stars occupy the nearly vertical strip at the size of the PSF, and are for the most part much brighter and smaller than galaxies. The magnitude and flux radius of objects reported as stars in the SDSS are shown in blue points. By performing a flexible clustering analysis on these SDSS stars we are left with (red points). We additionally require that our PSF stars lie inside 1σ contours in the color-color stellar locus and the 2-component shear plane, which further purifies the stellar sample (green points/lines) and allows identification of aberrations as seen in Figure 4.

each. We then fit a polynomial surface to the PCA coefficients to provide a map of the PSF across the focal plane for each exposure, as in Jee et al. (2007). Figure 4 illustrates the PSF model fitting and interpolation, where special care has been given to ensuring the edges of each chip are roughly continuous and unaffected by gaps in PSF data.

Once the PSF stars have been selected and modeled in each frame, the process of forward PSF convolution and shape estimation of galaxy images can begin. The shape measurement algorithm used in this study operates on each exposure and is a modified form of the one used in the DLS (Jee et al. 2016) called sFIT which won the GREAT3 gravitational lensing challenge (Mandelbaum et al. 2015). For each galaxy the algorithm fits an elliptical Gaussian jointly across all exposures, convolved with the spatially resolved PSF extrapolated to the position of the galaxy in each frame.

As a consistency check, we investigate the agreement between wavelength bands on the final measured ellipticity profile, shown as colored lines in Figure 5. Also plotted (black line) is a model of the tangential shear of background galaxies according to an NFW profile with mass, concentration, and redshift of $M = 5 \times 10^{14} M_\odot$, $c = 4$, and $z = 0.55$. The thick shaded lines in Figure 5 represent the non-zero cross shear component measured in each filter, where their thickness is the 1σ width as measured in each bin and which are representative of the γ_t (thin line) errors. The same distribution of galaxies is used in the measurements of tangential and cross shear.

The consistency between bands implies that the weak

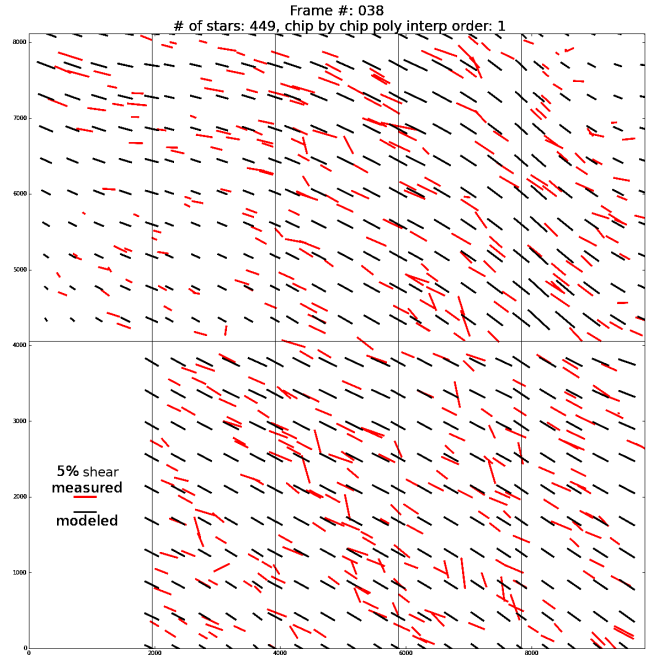


Figure 4. The observed (red) and PCA model (grey) of shear of PSF stars in one exposure before PSF correction. Ellipticity patterns induced by both telescope drift and optical aberrations are visible at the few percent level. Bright stars which were chosen for PSF modeling but which exhibited blooming (the outlier red whiskers) were rejected from the polynomial PCA coefficient modeling and interpolation.

lensing analysis can be improved ultimately by combining the information contained in multiple bands. For our shape estimation, each galaxy has its own shape measured in three bands, each of which is determined from the sFIT algorithm using PSF stars in that band's exposures. The shape agreement between bands is then used to provide an estimate of the error on shape measurement, which is then used as a weight in later analysis including mass mapping and correlation function measurements.

2.3 HST observations

The Lynx field has been the subject of multiple previous investigations, including deep Hubble observations weak lensing analysis by Jee et al. (2006). In that paper, a shapelet decomposition method is used to measure the shear, providing a useful cross-check for our own systematics in the Subaru data. The HST shape catalog was used in the 3σ detection of two $M \sim 2 \times 10^{14} M_\odot$ members of the $z \sim 1.3$ super cluster Lynx-E and W, which have been well-studied and verified with Chandra X-ray analysis in addition to the weak lensing mass. We match this space-based shape catalog with the photometry provided by the Suprime-cam observations, and then map the E- and B-modes as was performed with the ground-based data. These space and ground-based shears are then compared, as discussed below. The HST imagery we analyze unfortunately does not cover the central region of Lynx North at $z \sim 0.55$, but its influence is easily observed in the shear field near the boundary. Indeed, the

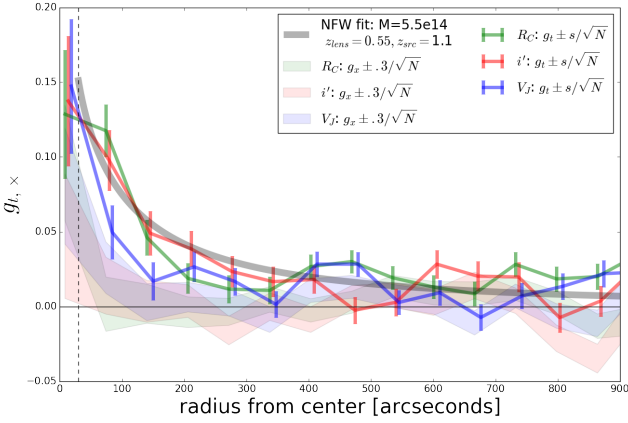


Figure 5. The reduced shear measured azimuthally around Lynx North cluster ($M = 5 \times 10^{14} M_{\odot}$ cluster at $z = 0.55$), as measured in the $V/R_c/i'$ wavelengths for sources with $z_{phot} > 0.9$. A model of the tangential shear induced on lensed sources at a median redshift of $z = 1.1$ is shown in black. The cross shears (filled color curves) displayed also agree between the bands, showing an anomalously low cross shear on the smallest scales which is not present in a singular NFW model. Error bars are computed from an assumption of intrinsic shape noise ($.3/\sqrt{N}$), as well as from the sample standard deviation in each bin (s/\sqrt{N}), where no bin overlap or smoothing has been applied. An estimate for the Einstein radius of the cluster is shown as the vertical dashed line.

tangential shear about the coordinates of Lynx North (outside of the HST observations) is virtually identical with both the shears as measured in the Suprime-cam observations and the model shown in Figure 5. This implies a good signal in the mass mapping algorithm as well, which we describe in the next section.

3 MASS MAPPING

In N-body simulations and theories of the formation of large scale structure, the clumping of matter forms in a hierarchical manner with a well-defined and characteristic mass density profile for clusters of galaxies (Navarro et al. 1997). We use this to apodize a shear statistic in order to locate and map overdensities along the line of sight. One such statistic is the aperture mass statistic M_{ap} first introduced in Schneider (1996):

$$M_{ap}(\theta) = \int Q(|\theta|) \gamma_t(\theta) d^2\theta \quad (1)$$

This function takes the background galaxy shears around each point in a map and filters them with the function Q . The optimal filter is the form of the expected tangential shear signal induced by the characteristic NFW mass profiles, as given in Wright & Brainerd (2000). This tangential shear profile can be approximated as an apodized combination of exponentials and hyperbolic tangent functions which can be scaled to match clusters of varying mass and lensing efficiency. This useful approximately-NFW fil-

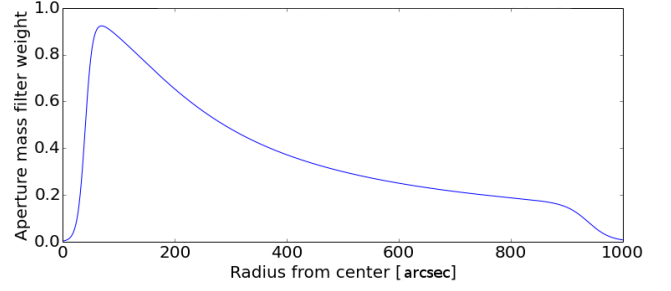


Figure 6. The apodization of the tangential shear of a massive foreground cluster. This function is defined as Q in Equations 2 and 3, and is used to filter tangential shears and form maps of signal to noise as in Equation 4.

ter function was introduced in Schirmer et al. (2007), and is given by Equation 2.

$$Q_{NFW}(x) = Q_{box}(x) \frac{\tanh(x/x_c)}{x/x_c} \quad (2)$$

The parameter x is a dimensionless radius: the angular separation in units of the cutoff radius r_{out} , i.e. $x := r/r_{out}$, and x_c is a dimensionless parameter that controls the rate of tangential shear decrease (concentration) in the NFW profile, and is taken to be $x_c \sim 0.15$. The apodization function Q_{box} provides the exponential damping around zero radius and around the cutoff radius r_{out} and is given by:

$$Q_{box}(r) = (1 + e^{6-150r/r_{out}} + e^{-47+50r/r_{out}})^{-1} \quad (3)$$

The resulting form of the Q_{NFW} filter is shown in Figure 6.

Due to the WL mass-sheet degeneracy, convergence or mass density maps are measured by subtracting a reference shear from the measured shear, and thus are bipolar. Such maps are often thresholded at some positive level in order to display positive mass. Rather than picking thresholds or contours arbitrarily, we choose instead to plot aperture mass signal-to-noise ratio. Significance of mass density peaks may then be readily assessed. We spatially map the aperture mass signal-to-noise S_t by dividing M_{ap} by the correspondingly apodized shape shot noise with an average RMS source galaxy shear of $\sigma_e \sim 0.3$. This denominator is equivalent to computing the statistic in a field with no lensing. This can be represented discretely as:

$$S_t = \frac{\sqrt{2} \sum \epsilon_{t,i} w_i Q_i}{(\sum (\sigma_e w_i Q_i)^2)^{1/2}} \quad (4)$$

Peaks in this S_t map correspond to locations where the tangential shear is largest and most similar to an NFW mass profile, which most likely correspond to clusters or groups of galaxies in the foreground. The most massive structure in our field, the cluster Lynx North (previously detected and measured in Miyazaki et al. (2007)) is detected at $S/N > 10$ in all three shape catalogs V, R_c, i' . The combined S/N map is shown in Figure 7, where contours colored from blue to red indicate S_t from -3 to 8. The contours indicate the complexity of the mass clustering in the field of view and overlay an RGB (i', R_c, V band) image of the region near Lynx North. Red sequence galaxies in this region, indicators

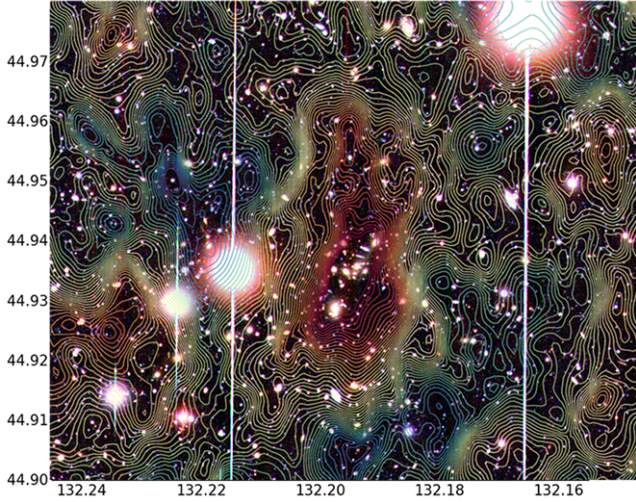


Figure 7. Zoom into 5 arcminute subfield RGB image of the Lynx North cluster at $z = 0.55$, with mass map contours overlaid, where blue to red contours go from S_t of -3 to 8, as defined in Equation 4. The bands used are the i' , R_c , and V for the RGB colors, respectively. Structures of foreground red cluster sequence galaxies are often observed to correlate with the E-mode shearing of background galaxies (those with $z_{phot} > 0.8$).

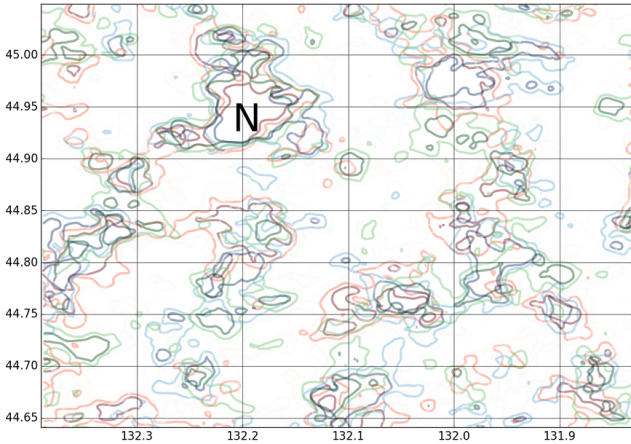


Figure 8. Aperture mass (E-mode) map of the Lynx field, with blue, red, and green contours corresponding to the i' , R_c , and V band shapes respectively. Shot noise normalized mass mapping is performed using sources with photo $z > 0.8$, and contours range from $0 < S_t < 3$

of cluster membership, often underlie areas of positive S_t across the entire field.

The mass maps in all three bands are shown as contours in Figure 8. They are correlated. Calculating the Pearson correlation coefficient using the E-mode maps in the V , R_c , i' bands gives $\rho_{R_c, i'} = 0.5156 \pm 0.0005$ and $\rho_{R_c, V} = .4789 \pm .0003$, where the errors have been estimated from bootstrap resampling.

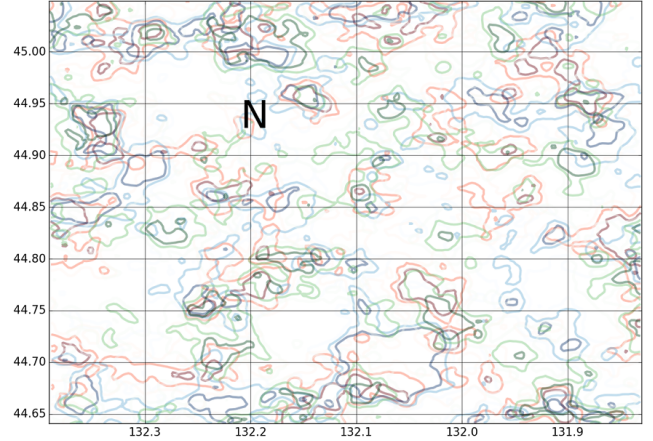


Figure 9. Cross aperture mass (B-mode) map of the Lynx field, with blue, red, and green contours corresponding to the i , R , and V band shapes. Shot noise normalized mass mapping is performed using sources with photo $z > 0.8$, and contours range from $0 < S_\times < 3$

3.1 Observational B-modes

One can use the cross shear γ_\times , instead of the tangential shear in Equation 1 to define the cross statistic S_\times .

$$S_\times = \frac{\sqrt{2} \sum \epsilon_{x,i} w_i Q_i}{(\sum (\sigma_e w_i Q_i)^2)^{1/2}} \quad (5)$$

In this case, the weighting function Q is not an optimal filter for detection because there is no cross shear in a single isolated NFW concentration. Nonetheless, this B-mode statistic can be computed easily and is often used as a check for systematic errors. Presence of significant B-modes in weak lensing studies can be caused by PSF mis-estimation. It is usually therefore assumed that if PSF correction is done properly (and there are no astrophysical sources of B-modes), these maps should be consistent with noise. As shown in Figure 9, our S_\times map shows clearly spatially correlated structure which is consistent across the VRi bands. Since the PSF was estimated separately for each band, it is unlikely that the origin of this cross-band common B-mode is PSF error. The Pearson correlation coefficient for the B-mode maps in the R/i and R/V maps is $\rho_{R,i} = 0.289 \pm 0.004$ and $\rho_{R,V} = 0.363 \pm 0.003$, where the error bars have been estimated from bootstrap resampling.

The significance of the correlation between multiple bands suggests a non-PSF related source for the B-modes, since the observations in multiple filters were completely independently measured and observed on nights separated by many months and vastly different stellar PSF patterns. In the next section, we examine how these modes are an astrophysically interesting signal, beyond their typical use as a measure of systematic error.

3.1.1 HST validation

As mentioned above, we also analyze a small region of HST ACS imagery as first presented in Jee et al. (2006), which has a different orientation, camera, optics, shape measurement scheme, and is free of atmospheric effects, reducing the pos-

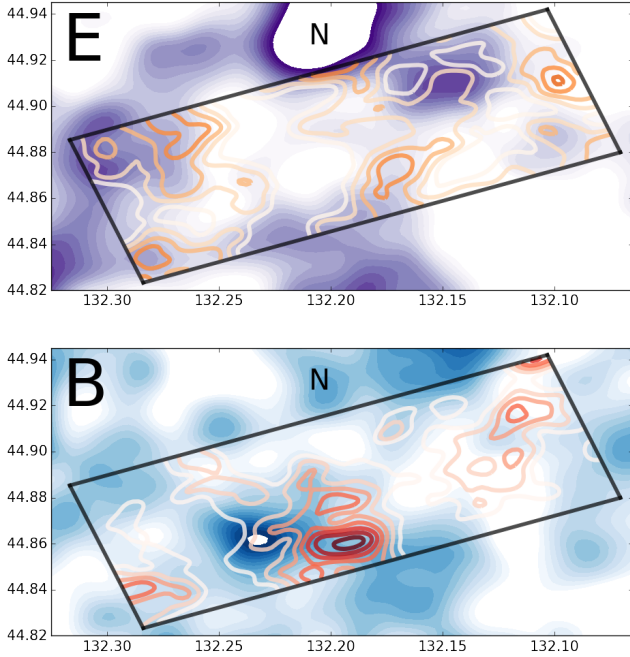


Figure 10. Comparing E- and B-mode maps of a portion of the Lynx field as observed from both the ground and space (the black boundary represents 3 HST ACS dithers). Top: the E-modes observed around Lynx-North, where purple shading and orange contours are the maps from the ground and space, respectively. Bottom: the B-modes, where blue shading and red contours are the B-modes from the ground and space. Both maps show general agreement despite different PSF conditions, shape modeling algorithms, and boundary sizes. The shading and contours in both the E- and B-mode maps range from $-1 < S < 4$.

sibility of systematic B-modes induced or contaminated by these effects showing up in the Suprime-cam maps. Overlays of the E- and B-mode maps from Subaru and HST are shown in Figure 10, showing good correspondence between the E- and B-modes. Notably, the effects of Lynx North can be seen intruding on the northern edge of the HST field, shown in red contours, as well as other clusters in the field. As for the B-modes, though there is disagreement on small-scales the general agreement is also apparent in the correspondence between shaded ($B > 0$) and unshaded ($B < 0$) regions of the map. This space-based observation validates the shape analysis and mass mapping algorithm used in the analysis of the ground-based data, indicating that the maps are likely not biased on large scales by observational effects due to the atmosphere, optics, or shape measurement algorithms.

4 LENS MODELING OF THE E & B MODES

To investigate further the origins of B-mode, we simulate these observations in a controlled way in 3D using the actual foreground mass distribution with a variety of simulated source galaxy distributions. Lynx North, as the most massive cluster in the observed field, is easily detected as an extended peak in the E-mode map (Figure 8) with $S_t > 10$ in each observed filter. There are also many extended regions of lower signal to noise peaks in the mass map which

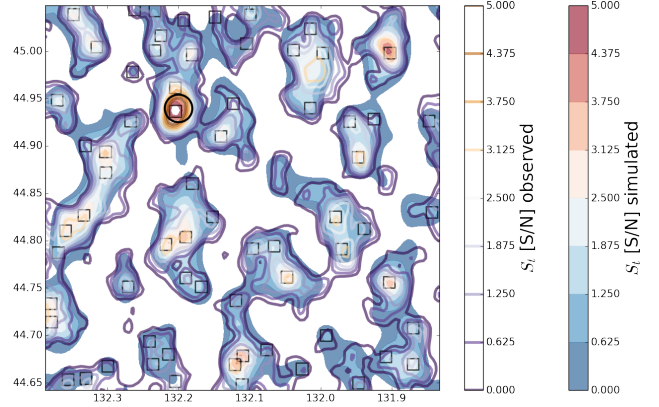


Figure 11. Simulated and observed E-mode maps, shown as filled contours and lined contours respectively. Locations of detected halos in the field above $S_t = 2$ shown as empty black squares. The simulated and observed maps are highly correlated.

are also detected in multiple filters and which most likely correspond to foreground structures of lesser mass or lensing efficiency. We compute a $S_{t,sim}$ map for an NFW profile, using the mass as a free parameter and estimating the cluster redshift and concentration parameter from the data. This fitting is performed simultaneously for all peaks in the observed S_t map with $S_t > 2$. The mass is therefore estimated from the comparison of the simulated map and the observed map, and the redshift of the cluster is estimated from the histogram vs redshift of the foreground galaxy density along the line of sight. The concentration parameter is assumed from a mass-concentration relation in Duffy et al. (2008). We do this fitting simultaneously for $N_{clust} = 128$ E-mode peaks as indicated by boxes in Figure 11, which are correlated with foreground lensing clusters or groups of galaxies. Though some of these assumed peaks may not correspond to real halos, and the real halos may not have exactly NFW shear profiles, their strength, spatial distribution, and number density above $M = 10^{13} M_\odot$ is similar to what is expected in similarly-sized fields (see Appendix for application to Λ CDM N-body large scale structure simulations).

We then model the shear of all background ($\sim 1 \times 10^4$ galaxies with $z_{phot} > 0.8$) as being the sum of shears by all halos in the foreground. This is done by taking each background galaxy located in 3-dimensional coordinate space RA/Dec/z and computing the total reduced shear g_{tot} as the sum of all the shears induced by the predicted foreground halos. The reduced shear of background galaxies around each halo is computed using the shear from a single NFW mass distribution (Wright & Brainerd 2000). Input parameters include the mass, concentration, and 3-d positions of the lens and source (as well as cosmological parameterizations of $h = .68$ and $\Omega_\Lambda = .7, \Omega_m = .3$ which determine angular diameter distances). The total shear g_{tot} for each background source is then given by the sum:

$$g_{tot} = \sum_j g_j(M_j, z_j, c_j, \delta_r, z_{source}) \quad (6)$$

where the sum is taken over all halos, j which lie in the foreground of the lens and where δ_r and is the estimated

angular distance between source and halo and z_{source} is the photometric redshift of the source. The resultant reduced shear sums for each galaxy in the simulation can then be compared to the observed shears. Since the simulations are shape-noise free, the reduced shears in the simulation are mostly of an amplitude $g_{1,2} < 0.1$ in correspondence with the weak lensing limit being applied here. The correlation of shear components of the simulations and observations is weak but statistically significant, $\rho_{e1:sim,obs} = 0.084 \pm 0.004$ and $\rho_{e2:sim,obs} = 0.088 \pm 0.014$. Adding a shape noise (pre-lensing) broadens the $e_{1,2}$ distributions to the observed values degrades the correlation between simulated and observed shears.

The simulated shears can then be run with same aperture mass mapping algorithm as described in the previous section to produce simulated maps, and then compared to the observed maps. This spatial correlation is shown in Figures 11, 12, and 13. The correlation coefficient of the simulated E- and B-mode maps with the observed maps is $\rho_{E:sim,obs} = 0.83 \pm 0.02$ and $\rho_{B:sim,obs} = 0.22 \pm 0.01$, which can be seen graphically in Figure 13. The E-mode correlation is quite strong, as it should be because we have iteratively fit the foreground halos to match the observed tangential signature maps. The simulated and observed B-mode maps also have statistically significant correlations, but at a weaker level. This is because the B-mode amplitudes in our noise-free simulation are much smaller than those in the observed field.

If random shape noise is included in the forward simulation by introducing an rms noise into each background galaxy at an amplitude of $\eta_{rms} = 0.3$, it is found that that the $1\text{-}\sigma$ width of the simulated S_t and S_\times distributions nearly match the width of the observed S_t and S_\times distributions as seen in Figure 14. In confirmation, when random shape noise is added, the Pearson correlation coefficient of the E- and B-modes ($\rho_{E:sim,obs}$, $\rho_{B:sim,obs}$) are lessened, but the correlation still remains statistically significant.

Beyond those induced by shape noise, there are other sources of observational B-modes at play here. The largest and most mundane source of B-modes are those induced at the boundaries of the aperture mass map, where pure E-modes can leak into the B-mode when aperture measures are used (azimuthal symmetry violation). These B-modes can be mitigated by padding the edges of the simulation or by limiting consideration of B-modes near the edges entirely. However, these edge B-modes are related to the strengths and locations of the lenses in the field, and therefore are not entirely noise. Another source of B-modes is the clustering of source galaxies, as discussed in Schneider et al. (2002) and Yu et al. (2015). These variations in spatial positions of galaxies leads to an asymmetry in aperture measurements of pure E-mode fields, and again are completely describable if the known positions of E-modes are known.

We can probe and eliminate these two galaxy density effects in a simulation by using a uniform distribution of galaxies at a fixed redshift which are lensed by the estimated 3D positions of halos. If we map the E- and B-modes using an extended uniform distribution of galaxies (at a single source plane of $z = 1.0$) such that no cluster is within several aperture radii of the extended galaxy boundary, the edge effect disappears and the correlation with the observed B-mode map is greatly reduced. However, as shown in Fig-

ure 14, there are still non-zero B-modes even in the case of uniform source galaxy distributions.

The B-modes which remain after edges and source non-uniformity effects are removed are perhaps more physically interesting, as they can be a sign of multiple lensing of background galaxies. For instance, the B-mode patterns induced by two massive cluster lenses projected along the line of sight produces an asymmetric quadrupole pattern as discussed in Bertin & Lombardi (2001). However, the simulated source galaxy density in their study was much higher than our current ground observations allow, and their simulations only include very fortuitous alignments of clusters along the line of sight. Therefore, we do not expect such obvious B-mode patterns in our observations, and they aren't readily seen in our observed maps. However, in our simulations we can probe this multi-lensing effect by modifying the distribution of lenses and galaxies. In fact, it is observed that the width of the S_\times distribution is broader in the case of realistic 3D lens positions than when all lenses are placed at a single redshift. Additionally, if the source galaxy density is greatly increased to $n_{gal} = 100 \text{ arcmin}^{-2}$, the width of the S_\times distribution is increased even further and the quadrupolar B-mode pattern of double lensing (Bertin & Lombardi 2001) is observable in the maps. In practice, this multi-lens effect broadens the simulated (and observed) S_\times distribution by a small amount, but given the much lower surface density of $z > 0.8$ galaxies in our observations, the effect of double lensing in this field is unresolvable.

Finally, there are B-modes in the observed $V/R_c/i'$ maps which have larger amplitudes than can be accounted for by our lensing simulation. These stronger B-modes, shown as the excess of gray shaded area over the blue line in Figure 14, might be accounted for with more realistic simulation of the lensing potential distribution which we can only approximate. For instance, in the simulation we do not include void lensing, which would increase the number of negative E-modes and likely contribute positive and negative B-modes. Additionally, on the smallest and largest scales the finite field of view, our observations limit the size of E-modes which are measurable with our data, and this necessarily limits our E- and B-mode simulation which are constrained in this way by the observations. Lensing on scales less than $\sim 1 \text{ Mpc}$ and scales which span the entire field of view, those larger than $\sim 100 \text{ Mpc}$, are therefore unaccounted for in our finite field reconstruction. B-modes may be induced by lenses outside the field.

4.1 Shear correlation functions

Statistical correlations are complimentary to spatial maps. While losing spatial information, the summary statistics produced by correlating the shears of all galaxies can provide a less noisy test of the origins of B-mode. Correlation functions over the field are computed using both the observed shears and those simulated under multiple conditions. The shear correlations ξ_\pm , the E- and B-mode aperture mass dispersion $\langle M_{ap,\times}^2 \rangle$, and tophat shear $\langle \gamma^2 \rangle_{E,B}$ dispersion are calculated on scales of $0.5 < \theta < 15 \text{ arcminutes}$. The raw shear correlation function is computed by correlating the tangential and cross shear around each galaxy, and either

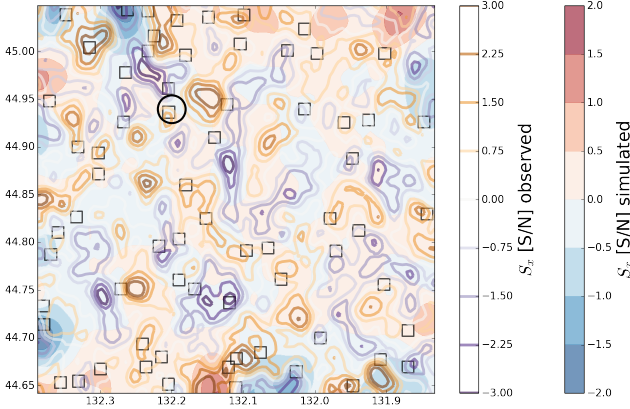


Figure 12. Simulated and observed B-mode maps, represented as filled contours and lined contours respectively. Location of Lynx North is indicated by the circle, and other subclusters are located as in Fig 11. By eye, there is a weak correlation between the contours and the shading, which is measured to be statistically significant. The generation of weak lensing B-modes by introduction of a pure E-mode field is apparent.

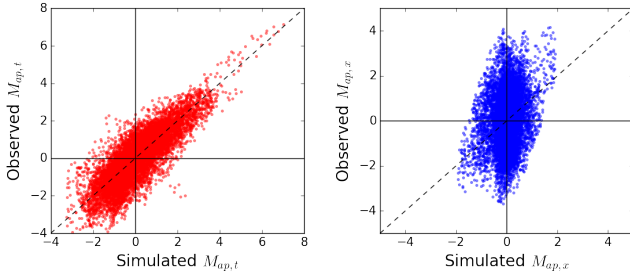


Figure 13. The correlation between the observed (ordinate) and simulated (abscissa) aperture mass mapping pixels for the E- and B-modes. B-modes presented are with masking out the edges by 10%, which does not significantly reduce the correlation. The simulation included the full lens distribution and realistic galaxy positions. Addition of shape noise in the simulation broadens the B-mode distribution (see Fig 14) and slightly reduces the correlation.

summing or differencing the two correlations.

$$\xi_{\pm}(\theta) = \langle \gamma_t \gamma_t \rangle \pm \langle \gamma_{\times} \gamma_{\times} \rangle \quad (7)$$

These raw correlations depend on both the E- and B-mode power spectrum, and so the decomposition into aperture mass statistics is a useful one. We define the aperture mass correlations in terms of the ξ_{\pm} functions generally as:

$$\langle M_{ap,\times}^2 \rangle(R) = \int_0^\infty \frac{r dr}{2R^2} \left[T_+ \left(\frac{r}{R} \right) \xi_+(r) \pm T_- \left(\frac{r}{R} \right) \xi_-(r) \right] \quad (8)$$

where M_{ap} and M_{\times} take the plus and minus signs, respectively, and the functions T_{\pm} are window functions which are generalized autocorrelations of the filter function Q , and which limit the inclusion of small and large radii which are difficult to measure. Previously in Section 3 we chose Q to be a signal-matched filter (NFW-like) for optimal detection

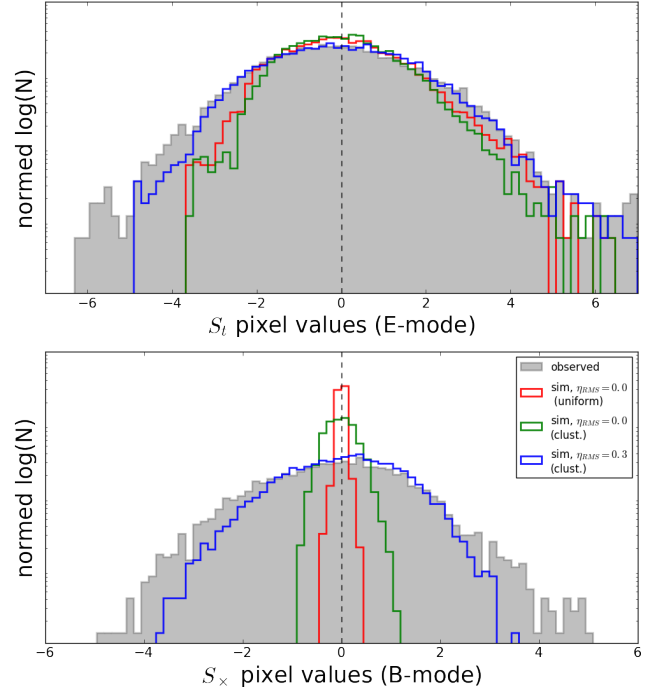


Figure 14. The distribution of E- and B-mode map pixel values. Red lines show the simulated shears of a uniform (homogeneous) source plane of galaxies at $z = 1.0$ that fill the observed field of view. Green lines use the actual (inhomogeneous) distribution of source galaxies, which with the addition of shape noise form the blue lines, better match the observed distributions (shaded). B-mode distributions are shown without edge effects, indicating the presence of multiple lensing B-modes in the uniform galaxy simulation.

of E-modes, but for the correlation functions presented here we use a Gaussian-derivative type window function which give T_{\pm} in the form:

$$T_+(s) = \frac{s^4 - 16s^2 + 32}{128} \exp(-s^2/4) \quad (9)$$

$$T_-(s) = \frac{s^4}{128} \exp(-s^2/4) \quad (10)$$

$$(11)$$

as presented in Crittenden et al. (2002).

Another popular cosmic shear statistic is the shear dispersion within a circle of radius R , which can again be decomposed into the shear-shear correlations as given by the expression:

$$\langle \gamma^2 \rangle_{E,B}(R) = \int_0^{2R} \frac{r dr}{2R^2} \left[S_+ \left(\frac{r}{R} \right) \xi_+(r) \pm S_- \left(\frac{r}{R} \right) \xi_-(r) \right] \quad (12)$$

where the E- and B-modes correspond to the + and - in the equation on the R.H.S. These E/B decompositions of the shear field are also filtered analogously to $\langle M_{ap,\times}^2 \rangle$, but with the S_{\pm} window functions applied as follows:

$$S_+(s) = \frac{1}{\pi} (4 \arccos(s/2) - s\sqrt{4-s^2}) \quad (13)$$

$$S_-(s) = s\sqrt{4-s^2}(6-s^2) - 8(3-s^2) \arcsin(s/2) / (\pi s^4) \quad (14)$$

$$(15)$$

for $s \leq 2$, and $S_-(s) = 4(s^2 - 3)/(s^4)$ for $s \geq 2$. These

window functions are broader than T_{\pm} , implying that more shear dispersion signal is included but the signal is less localized. A constant shear generates contributions to both E- and B-modes (Schneider et al. 2002).

The correlations are computed on our dataset using the **TreeCorr** code (Jarvis et al. 2004), and the results are displayed in Fig 15. Three separate shear datasets are shown: the observed shears, those simulated with uniform source plane at $z = 1.0$ at a galaxy number density of 11 arcmin^{-2} , and those simulated using the observed $RA/Dec/z$ positions on the sky. E- modes for each statistic are the upper curves in each subplot in purple shades, and B-modes are shown in shades of aqua. Error bars on the observed correlation functions are from purely shape noise with an $\eta_{rms} = 0.3$, and the simulated cases have no noise added. As a null test, randomizing the shear components but keeping the positions fixed resulted in zero correlation in all statistics at all scales.

This field has extensive large scale structures which give an average matter density in excess of that given by the universal mass power spectrum. Thus the correlation functions as computed on this limited field reach large values, as expected from the depth of the field and the abundance of clustering along this line of sight. Interestingly, there are also non-zero B-mode correlations, which ordinarily might be blamed on incomplete modeling of the PSF or gaps in the data. However, there are B-modes of similar amplitude in each correlation function even when there is no masking and a uniform lens plane is used. This implies that the majority of observed B-modes are not due to a PSF modeling issue or even the clustering of source galaxies, but rather are intrinsic to these particular decompositions of a realistic shear field into E- and B-modes.

One may worry about the edges of this field, in that there seems to be B-modes induced at the boundaries of the field due to incomplete sampling of cluster-induced E-modes. However, since the correlation functions ξ_{\pm} are directly sampled at each galaxy point and not on a grid (as in the mapping scenario), the edges are not an issue (Schneider et al. 2002). In fact, masking more ($\sim 5 \text{ arcmin}$) of the edges of the observation does not noticeably change the correlation function.

5 SUMMARY

In this paper we have explored the tomographic mapping of mass using measurements of shears and redshifts from a multi-band observations similar to what will be available with the LSST 10 year dataset. In this field the successive lensings of over a hundred massive lenses in a $.5 \times .5$ degree field are measured and simulated. Through both aperture mass maps and shear correlation functions we show that the decomposition of the observed shear field into gradient (E-modes) and curl (B-modes) yields useful results. By associating E-map overdensities with galaxy clusters along the line of sight we show that the patterns of pure tangential shear from such lenses induce a measurable B-mode. Contrary to a systematic error, these modes contain information about the clustering of source galaxies in relation to the distribution of foreground lenses inside and outside the field.

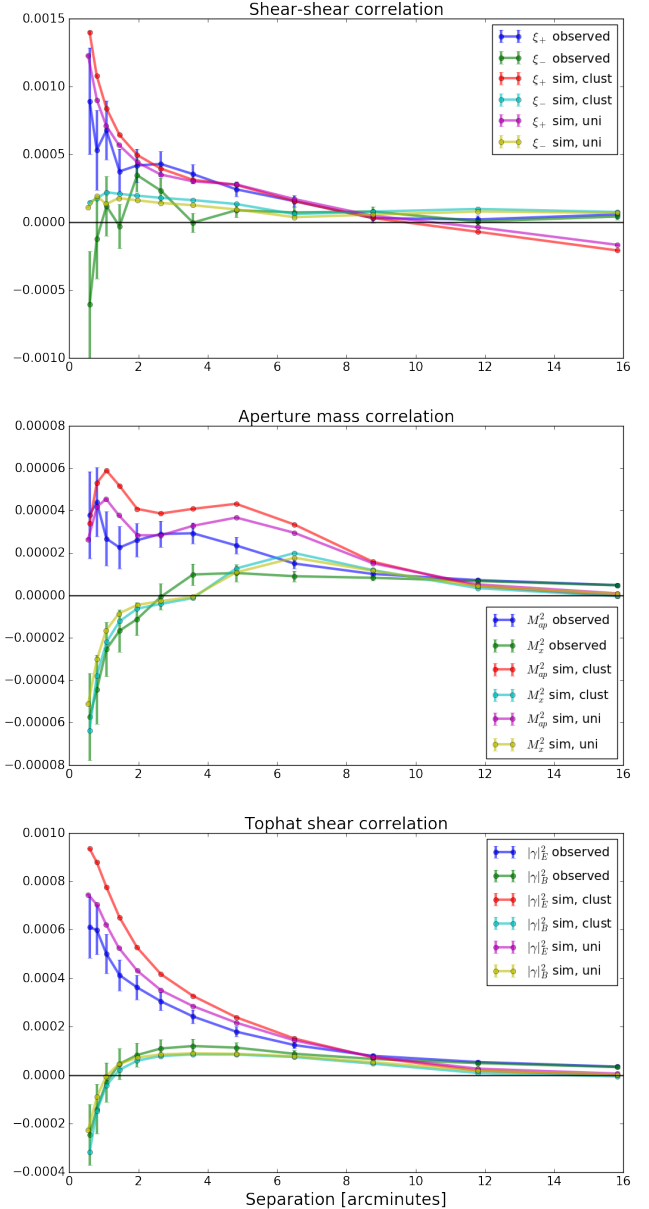


Figure 15. The three shear correlation functions for the Lynx field, ξ_{\pm} , $\langle M_{ap,\times}^2 \rangle$, and $\langle \gamma_{E,B}^2 \rangle$. In each panel, for each correlation function, three different sets of shears are correlated: 1) the observed shears and positions (which are clustered), 2) the simulated shears (which are lensed by multiple planes) and observed locations (in RA/Dec and z), and 3) a uniform background of galaxies at $z = 1.0$ with the same number density as the observations. This shows that in the case of the correlation functions, the observed B-modes are not just due to the clustering.

ACKNOWLEDGEMENTS

We thank Michael Schneider and Sam Schmidt for many helpful discussions. Financial support from DOE grant DE-SC0009999 and Heising-Simons Foundation grant 2015-106 are gratefully acknowledged. We thank Risa Wechsler, Joe DeRose, and the Buzzard simulation team for their N-body lensing simulation catalogs. M.J.J. acknowledges support for

current research from the National Research Foundation of Korea under the program 2017R1A2B2004644.

REFERENCES

- Antilogus P., Astier P., Doherty P., Guyonnet A., Regnault N., 2014, *Journal of Instrumentation*, **9**, C03048
- Baba H., et al., 2002, in Bohlender D. A., Durand D., Handley T. H., eds, *Astronomical Society of the Pacific Conference Series Vol. 281, Astronomical Data Analysis Software and Systems XI*. p. 298
- Bacon D. J., Refregier A. R., Ellis R. S., 2000, *MNRAS*, **318**, 625
- Bartelmann M., 1995, *A&A*, **303**, 643
- Becker M. R., 2013, PhD thesis, The University of Chicago
- Benítez N., 2000, *ApJ*, **536**, 571
- Bertin E., 2006, in Gabriel C., Arviset C., Ponz D., Enrique S., eds, *Astronomical Society of the Pacific Conference Series Vol. 351, Astronomical Data Analysis Software and Systems XV*. p. 112
- Bertin G., Lombardi M., 2001, *ApJ*, **546**, 47
- Bertin E., Mellier Y., Radovich M., Missonnier G., Didelon P., Morin B., 2002, in Bohlender D. A., Durand D., Handley T. H., eds, *Astronomical Society of the Pacific Conference Series Vol. 281, Astronomical Data Analysis Software and Systems XI*. p. 228
- Coe D., Benítez N., 2015, *ColorPro: PSF-corrected aperture-matched photometry*, *Astrophysics Source Code Library* (ascl:1508.005)
- Coe D., Benítez N., Sánchez S. F., Jee M., Bouwens R., Ford H., 2006, *AJ*, **132**, 926
- Cooray A., Hu W., 2002, *ApJ*, **574**, 19
- Crittenden R. G., Natarajan P., Pen U.-L., Theuns T., 2002, *ApJ*, **568**, 20
- DeRose J., Wechsler R., Rykoff E., et al., 2017, in prep.
- Duffy A. R., Schaye J., Kay S. T., Dalla Vecchia C., 2008, *MNRAS*, **390**, L64
- Guzik J., Bernstein G., 2005, *Phys. Rev. D*, **72**, 043503
- High F. W., Stubbs C. W., Rest A., Stalder B., Challis P., 2009, *AJ*, **138**, 110
- Hilbert S., Hartlap J., White S. D. M., Schneider P., 2009, *A&A*, **499**, 31
- Holden B. P., et al., 2001, *AJ*, **122**, 629
- Jarvis M., Bernstein G., Jain B., 2004, *MNRAS*, **352**, 338
- Jee M. J., White R. L., Ford H. C., Illingworth G. D., Blakeslee J. P., Holden B., Mei S., 2006, *ApJ*, **642**, 720
- Jee M. J., Blakeslee J. P., Sirianni M., Martel A. R., White R. L., Ford H. C., 2007, *PASP*, **119**, 1403
- Jee M. J., Tyson J. A., Hilbert S., Schneider M. D., Schmidt S., Wittman D., 2016, *ApJ*, **824**, 77
- Joachimi B., Semboloni E., Hilbert S., Bett P. E., Hartlap J., Hoekstra H., Schneider P., 2013, *MNRAS*, **436**, 819
- Kaiser N., 1992, *ApJ*, **388**, 272
- Kaiser N., Wilson G., Luppino G. A., 2000, *ArXiv Astrophysics e-prints*,
- Kilbinger M., 2015, *Reports on Progress in Physics*, **78**, 086901
- Mandelbaum R., et al., 2015, *MNRAS*, **450**, 2963
- Mei S., et al., 2012, *ApJ*, **754**, 141
- Melchior P., Sutter P. M., Sheldon E. S., Krause E., Wandelt B. D., 2014, *MNRAS*, **440**, 2922
- Miyazaki S., Hamana T., Ellis R. S., Kashikawa N., Massey R. J., Taylor J., Refregier A., 2007, *ApJ*, **669**, 714
- Navarro J. F., Frenk C. S., White S. D. M., 1997, *ApJ*, **490**, 493
- Ouchi M., et al., 2004, *ApJ*, **611**, 660
- Pen U.-L., Lee J., Seljak U., 2000, *ApJ*, **543**, L107
- Pitrou C., Pereira T. S., Uzan J.-P., 2015, *Phys. Rev. D*, **92**, 023501
- Rosati P., Stanford S. A., Eisenhardt P. R., Elston R., Spinrad H., Stern D., Dey A., 1999, *AJ*, **118**, 76
- Schirmer M., Erben T., Hettterscheidt M., Schneider P., 2007, *A&A*, **462**, 875
- Schmidt S. J., Thorman P., 2013, *MNRAS*, **431**, 2766
- Schneider P., 1996, *MNRAS*, **283**, 837
- Schneider P., 2005, *ArXiv Astrophysics e-prints*,
- Schneider P., van Waerbeke L., Mellier Y., 2002, *A&A*, **389**, 729
- Stanford S. A., Elston R., Eisenhardt P. R., Spinrad H., Stern D., Dey A., 1997, *AJ*, **114**, 2232
- Stebbins A., 1996, *ArXiv Astrophysics e-prints*, astro-ph/9609149,
- The Dark Energy Survey Collaboration 2005, *ArXiv Astrophysics e-prints*,
- Tyson J. A., Valdes F., Wenk R. A., 1990, *ApJ*, **349**, L1
- Van Waerbeke L., et al., 2000, *A&A*, **358**, 30
- Wittman D. M., Tyson J. A., Kirkman D., Dell’Antonio I., Bernstein G., 2000, *Nature*, **405**, 143
- Wittman D., Tyson J. A., Margoniner V. E., Cohen J. G., Dell’Antonio I. P., 2001, *ApJ*, **557**, L89
- Wright C. O., Brainerd T. G., 2000, *ApJ*, **534**, 34
- Yagi M., Kashikawa N., Sekiguchi M., Doi M., Yasuda N., Shimazaki K., Okamura S., 2002, *AJ*, **123**, 66
- Yu Y., Zhang P., Lin W., Cui W., 2015, *ApJ*, **803**, 46
- von der Linden A., et al., 2014, *MNRAS*, **439**, 2

APPENDIX A: APPENDIX: N-BODY SIMULATION VALIDATION

In this appendix we briefly describe the validation of our method using the N -body cosmology simulation Buzzard (DeRose et al. 2017). The Buzzard simulation provides Dark Energy Survey (The Dark Energy Survey Collaboration 2005) 5-year depth catalogs that include positions (RA/Dec/ z) and reduced shear (g_1/g_2) of galaxies computed from ray-tracing (using *CALCLENS* (Becker 2013)), as well as the mass M_{200} and positions of clusters. Using this information we can test the ideas presented in the body of this paper, namely the applicability of the approximation in Equation 6, and whether B-modes are observationally present. The first of these tasks will require estimating the background galaxy shears using the known locations of cluster masses, and then whether or not the B-modes observed in the simulation are the result of this shear.

Taking a small slice of the Buzzard universe, about a degree on a side, we find galaxies and clusters distributed in 3D as shown in Figure A1. There is a large cluster centered in the foreground of this slice as $z = 0.28$ with mass $M_{200} = 6.8 \times 10^{14} M_{\odot}$ which will serve as an anchor for our observations, as well as ~ 120 other clusters/groups with $M_{200} > 2 \times 10^{13} M_{\odot}$ which will also be used into the lensing simulation. If we then slice the galaxy catalog by choosing galaxies only with $z_{photo} > 0.5$ (as shown in Figure A1) we should be able to easily detect this foreground cluster, given $\sim 40,000$ background galaxies with an observed number density of $n = 13$ background galaxies per square arcminute.

We first test the approximation of the shear of each background galaxy as the summation of the shears induced by the most massive clusters along the line of sight. This approximation is quite robust in the weak lensing limit, and clear comparisons between approximated shears and those computed from ray tracing the Buzzard simulation can be

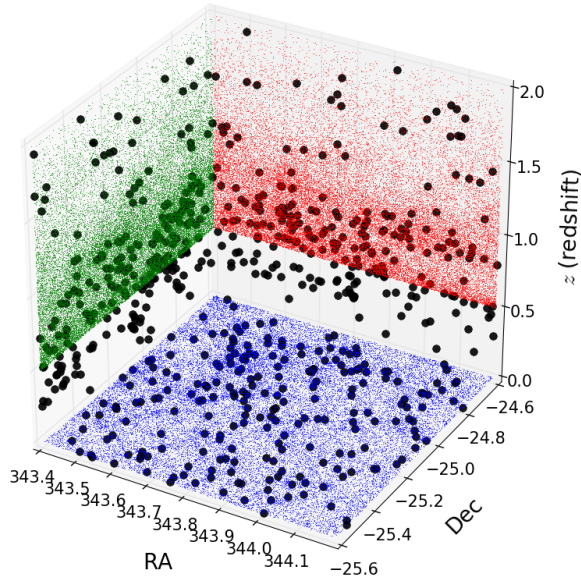


Figure A1. Three dimensional (RA/Dec/z) distribution of galaxies (colored dots) and clusters (black circles) in a small slice of the Buzzard simulation. Each side of the cube shows the projection of positions along two axes. All galaxies above the redshift cut of $z > 0.5$ are lensed by all foreground clusters.

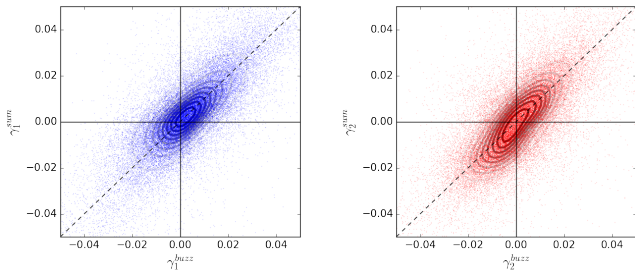


Figure A2. Comparing the shears as computed by **CALCLENS** and those from the re-simulation method described in the body. There is broad agreement between both the components of the shear, confirming the re-simulation’s usefulness. There is a slight offset in the field shear for the component g_1 which is seen in the ray-tracing and is captured in the re-simulation and is traceable to an asymmetry in the distribution of mass in the field.

seen in Figure A2. The broad agreement between both components of the shear indicates that the re-simulated shears are a good approximation to the ray-tracing ones, when given a catalog of foreground mass.

However, applying this technique to the sky necessarily means we must make our own catalog of massive clusters. In the observational frame, we are provided with measurements of the reduced shear (g_1/g_2) and RA/Dec/z of galaxies, and must find clusters using any combination of these parameters. To show the feasibility of this method in the Buzzard universe (and thus in the Lynx field), we automatically locate clusters by finding peaks in the map of the aperture mass statistic and estimate the unknown masses and red-

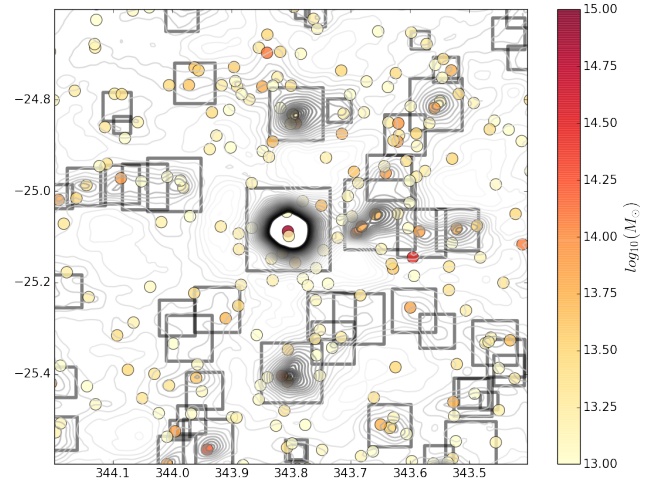


Figure A3. Segmenting the mass (S_t) map produced from filtering the Buzzard shears through the Equation 1 (S_t contours go from $1 < S_t < 4$). The boxes show the locations of detected peaks which are then fed into the mass measurement and re-simulation. Colored dots show the “unknown” locations of Buzzard halo catalog members with mass $M_{200} > 10^{13} M_\odot$.

shifts of the clusters from filtering the shears and through redshift clustering of foreground galaxies.

First, the peaks in the aperture mass map are located using an image segmentation process similar to that used in **SExtractor**. The resulting locations are shown in Figure A3. These putative cluster RA/Dec positions are associated with measurable overdensities in the provided (but unused) halo catalog, but which can be approximated through the use of photo- z estimates of foreground galaxies along the line of sight. In this way, the masses are estimated from a combination of tangential shear profile fitting and correlations between observed M_{ap} signal-to-noise and M_{200} (Schneider (2005)). The resulting correlation between this predicted mass and mass measured from the Buzzard N-body simulation is shown in Figure A4.

Using these predicted cluster masses and locations, which are proportional to the actual lensing mass, we then re-simulate the shear of the background galaxies as the summation of the predicted cluster mass lensings (thus introducing only E-modes into the shear field). Application of Eq. 4 on these shears produces re-simulated M_{ap} and M_\times (E and B-mode) maps which we can then compare to the ones which utilize ray-tracing shears as seen in Figure A5. Both maps illustrate the presence of B-modes with realistic distributions of clusters and source galaxies. The overestimation of lensing mass seen in Figure A4 leads to a slight over-estimation of S_t and S_\times , however the overall pattern is seen to be correlated. The shear correlation functions can also be computed on this narrow region of the simulated sky, which can be seen in Figure A6 and show similar shape and scale.

The similarity between the two sets of shears, as re-simulated from the sum of lenses along the line of sight and those computed from ray-tracing an N-body simulation, represents an opportunity for a simplistic representation of observed shears as a sum of finite components. This method applied in the analysis of the Lynx field shears

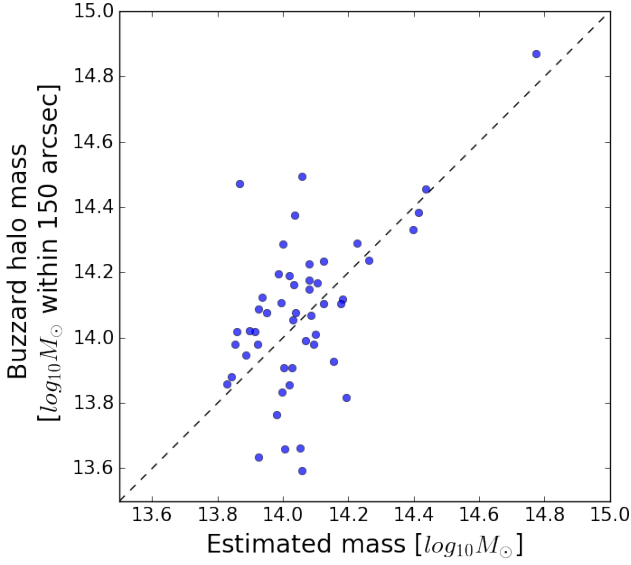


Figure A4. Estimation of lensing mass is performed through correlations between M_{ap} peak value, integrated S_t , and width (Eq. 19 of Schneider (2005)). The Buzzard halo catalog, which was not used in the detection or prediction on the abscissa, provides masses and locations which were summed in apertures of $150''$ to produce the actual lensing mass on the ordinate.

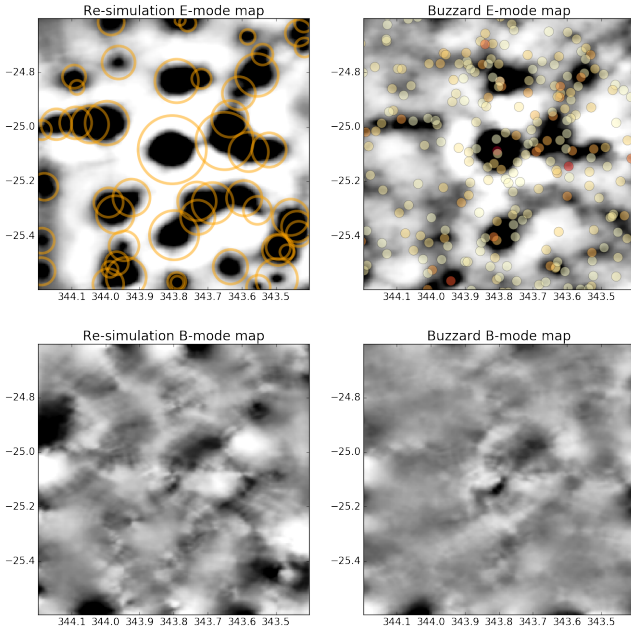


Figure A5. Comparison between the re-simulated and Buzzard ray-traced E- and B-mode maps, all color bars are $-1 < S < 1$ white to black. In the left column, maps are produced from shear computed by summing the tangential shear of masses estimated in Figure A4 at the locations indicated by open orange circles. On the right, shear is calculated through application of CAL-CLENS multiple-plane ray-tracing algorithm through the Buzzard N-body simulation. B-modes are present in both maps at similar amplitudes and locations.

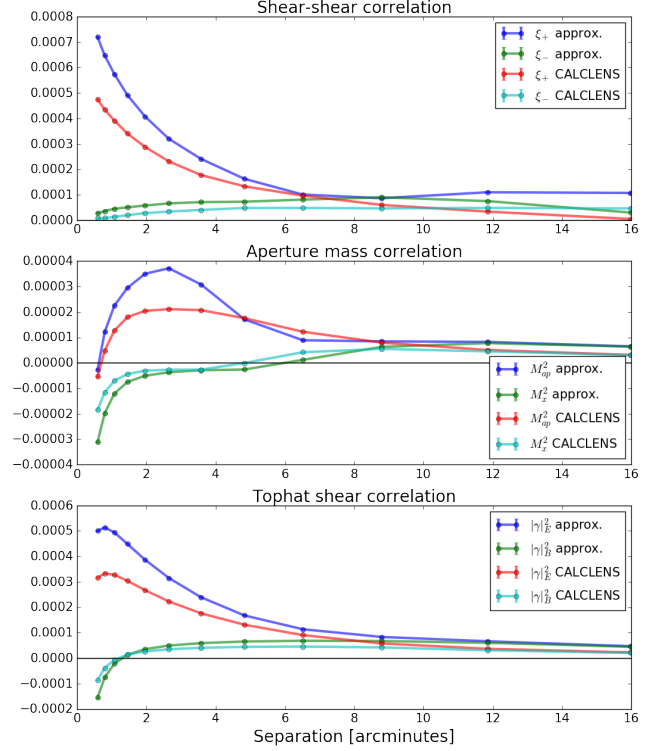


Figure A6. The three shear correlation functions for the re-simulated shears as compared to those from N-body ray-tracing. Shear-shear ξ_{\pm} , aperture mass $\langle M_{ap,\times}^2 \rangle$, and tophat shear $\langle \gamma_{E,B}^2 \rangle$ are shown in the top, middle, and bottom rows and defined in Eqs. 7, 8, and 12 respectively. In each panel the spatial correlations of the re-simulated and N-body ray-traced shears can be compared and found to be similar in amplitude, shape, and scale.

helps explain some of the observed B-modes in both spatial maps and overall correlations. These apparent observational B-modes, which are similar between the Lynx field and Buzzard simulations, can be understood from the combination of these analyses. Edge effects as well as inhomogeneous source galaxy positions lead to these apparent B-modes, which must be taken into account if the B-mode map is to be used as a test for systematics or new phenomena. These B-modes are not systematic errors resulting from PSF estimation or shape noise (neither of which are included in these simulations), but rather from the nature of spatial mapping and resulting correlation of shears of galaxies which are realistically distributed amongst, and then lensed by, a inhomogeneous 3-dimensional web of lenses.

This paper has been typeset from a \LaTeX file prepared by the author.